Anisotropy of interband transitions in InAs quantum wires: an atomistic theory

Marco Califano and Alex Zunger
National Renewable Energy Laboratory, Golden, CO, 80401

The electronic and optical properties of [001]-oriented free-standing InAs cylindrical quantum wires (QWRs) with diameters 10–100 Å are calculated using an atomistic, empirical pseudopotential plane-wave method. We analyze the effect of different degrees of mixing between valence bands on the optical properties of these nanostructures, by switching on and off the spin-orbit interaction. The fundamental transition in these QWRs exhibit a large anisotropy, with emission polarized prevalently along the wire axis z. The magnitude of such an anisotropy is found to depend on both degree of valence band mixing and wire size. In higher energy interband transitions, we find anisotropies close to 100% with emission polarized perpendicular to the wire axis. Furthermore, in large wires, transitions involving highly excited valence states show in-plane polarization anisotropies between the [110] and [1$\bar{1}$0] directions. InAs wires can therefore switch between z-polarized to xy-polarized emission/absorption for different excitation energies. This makes them ideally suited for application in orientation-sensitive devices.

PACS numbers: 71.15.-m, 71.55.-i

I. INTRODUCTION

Recent advances in fabrication techniques such as laser assisted catalytic growth (LCG) and its variations, made it possible[1-9] to produce high quality quantum wires (QWRs) of many III-V (InAs, InP, GaAs, GaP, GaN, etc), II-VI (ZnS, ZnSe, CdS, CdSe), and IV-IV (alloys of SiGe) semiconductors, with diameters ranging from 3 nm to several tens of nm, and lengths exceeding 1 μm. This growth method exploits laser ablation to generate nanometer diameter catalytic clusters that define the size and direct the growth of the crystalline nanowires by a vapor-liquid-solid mechanism. The availability of such perfect cylindrical samples at a crystalline level offers challenging opportunities to the theorist to explain their properties and predict new features that can be exploited for the realization of novel devices. One of the most important properties of QWRs is the polarization anisotropy of their interband transitions: due to the 1D confinement, the emission/absorption intensity $I_{\parallel}$ for light polarized parallel to the wire axis (z) can be different from that ($I_{\perp}$) for light polarized in the (x, y) plane, perpendicular to it. The polarization anisotropy is defined in terms of the degree of linear polarization

$$\rho = \frac{\alpha_{\parallel} - \alpha_{\perp}}{\alpha_{\parallel} + \alpha_{\perp}}. \qquad (1)$$

where α is the absorption coefficient. Furthermore, as the underlying crystal structure of the wire might be different along two perpendicular directions in the (x, y) plane, an in-plane polarization anisotropy can also be expected. A giant anisotropy in the band gap emission, which was found to be over 90% polarized parallel to the wire axis, was recently measured[1] in InP LCG-grown cylindrical wires. Interestingly, no transition polarized perpendicular to the wire axis was found[1] in an energy range of about 50-60 meV around the main peak. This feature makes the wires ideal for many orientation-sensitive applications, such as optical switches and interconnectors, near-field imaging and high resolution detectors. Moreover, the determination of the orientation of the polarization gives also specific indications on the optimal configuration of a QWR laser[10], i.e., on whether it is better to allign the wires parallel or perpendicular to the cavity walls in order to achieve maximum interaction with the optical cavity field.

The polarization of optical transitions in QWRs with different cross sections has been extensively studied both experimentally[11-15] and theoretically[16-26]. All studies concur to attribute the main origin of anisotropies in the dipole matrix elements of optical transition to valence band mixing. Another source of anisotropy in the optical transitions, that may occur even in the case of isotropic dipole matrix elements, is a dielectric constant discontinuity at the wire surface[22,23]. Although excitonic effects have also been found[27] to weakly contribute to the in-plane anisotropy even in cylindrically symmetrical quantum dots, this paper will focus only on the single-particle contribution to the polarization anisotropy in optical transitions. Despite the crucial importance of band mixing to optical anisotropy, most theoretical treatments[16-24] decouple conduction and valence bands, and consider only interactions between a limited number of valence bands, e.g., only between the bulk Γ_{8v}-derived heavy-hole (hh) and light-hole (lh) bands, neglecting coupling with the bulk Γ_{7v}-derived split-off bands. This approach is also known as the *infinite spin-orbit splitting approach*. Furthermore, in all the aforementioned treatments, the wire is assumed to be a *continuous* medium (i.e., with no underlying atomistic structure), modeled as a 2D square well. It has therefore an ideally high symmetry: $C_{\infty v}$ for a circular, C_{4v} for a square and C_{2v} for a rectangular cross-section, whereas the actual (atomistic) symmetries might be lower depending on the wire orientation.

In the present work we present an atomistic study of the electronic and optical properties of zinc-blende, [001]-oriented, free-standing cylindrical wires by means of a

semi-empirical pseudopotential method that naturally includes general multi-band coupling as well as the effect of spin-orbit (SO). In one set of our calculations, we also set artificially $\Delta_{so} = 0$ in order to study the contribution of the split-off bands to band mixing and consequently to polarization properties. We find that:

(i) the *fundamental* $h_1 \rightarrow e_1$ *transition* in QWRs shows a high polarization anisotropy, with emission polarized prevalently along the wire axis z. The magnitude of the anisotropy depends on the degree of valence band mixing: when the SO interaction is set to zero (i.e., for maximum band mixing), the value of the degree of linear polarization is close to 100% and is independent of both size and temperature; when a realistic value for the SO splitting is considered (i.e., for reduced band mixing), ρ decreases to about 80% and becomes size- and temperature-dependent.

(ii) *Higher energy interband transitions* show polarization anisotropies close to 100% with emission perpendicular to the wire axis, with no dependence on wire size or band mixing.

(iii) If we assume a line broadening of the order of that obtained in typical experimental conditions[1], the features of photoluminescence (PL) peaks with emission polarized perpendicular to the wire at energy close to the band gap transition are hidden by the broad band-gap PL. This might be the reason why no transition polarized perpendicular to the wire axis was found[1] in InP wires in an energy range of about 50-60 meV around the main peak.

(iv) Transitions involving highly excited valence states in thick wires show in-plane polarization anisotropies (i.e., anisotropies between the inequivalent [110] and [1$\bar{1}$0] directions, both perpendicular to the wire axis) regardless to whether SO is considered or not.

II. ORIGINS OF THE LINEAR POLARIZATION ANISOTROPY IN QWRS

Within the dipole approximation, in the limit where the wavelength λ of the electromagnetic field is much larger than the wire radius R, absorption and emission are proportional to the scalar product of the local electric field $\mathbf{E}$ and the interband dipole moment $\mathbf{p}$, averaged over the electron-hole wave function. The absorption coefficient α can therefore be written as:

$$\alpha^{(i)} \propto \frac{|\langle\psi_v|\mathbf{E}^{(i)}\cdot\mathbf{p}|\psi_c\rangle|^2}{|\mathbf{E}_\infty|^2}, \tag{2}$$

where $i = \parallel, \perp$ are the component parallel and perpendicular to the wire axis respectively. There are two main factors that can cause a polarization dependence in the optical transitions in a QWR: (i) a discontinuity in the dielectric constant between the wire and its surroundings[22,23]; (ii) a strong valence band mixing[20].

A. Polarization anisotropy due to dielectric constant discontinuity

According to Landau theory of dielectric media[32], when the electric field $\mathbf{E}_\infty$ of the incident light wave far from the wire is perpendicular to the wire axis, the amplitude of $\mathbf{E}$ inside the wire is strongly modulated on the scale of the nanostructure radius, due to the boundary conditions, resulting in[32]:

$$\mathbf{E}^\perp = \delta\cdot\mathbf{E}^\perp_\infty \tag{3}$$

where

$$\delta = \frac{2\varepsilon_{out}}{\varepsilon_{out}+\varepsilon_{in}}, \tag{4}$$

and ε_{in} and ε_{out} are the dielectric constant of the wire and the surrounding material, respectively. When $\mathbf{E}_\infty$ is parallel to the wire axis, no modulation takes place. The degree of linear polarization is defined as:

$$\rho = \frac{\alpha^\parallel-\alpha^\perp}{\alpha^\parallel+\alpha^\perp} = \frac{|\langle\psi_v|\mathbf{E}^\parallel\cdot\mathbf{p}|\psi_c\rangle|^2 - |\langle\psi_v|\mathbf{E}^\perp\cdot\mathbf{p}|\psi_c\rangle|^2}{|\langle\psi_v|\mathbf{E}^\parallel\cdot\mathbf{p}|\psi_c\rangle|^2 + |\langle\psi_v|\mathbf{E}^\perp\cdot\mathbf{p}|\psi_c\rangle|^2} \tag{5}$$

where we assumed $\mathbf{E}^\parallel_\infty = \mathbf{E}^\perp_\infty$. If $\mathbf{E}$ is homogeneous inside the wire, Eq. (5) becomes:

$$\rho = \frac{|M^\parallel_{cv}|^2 - \delta^2|M^\perp_{cv}|^2}{|M^\parallel_{cv}|^2 + \delta^2|M^\perp_{cv}|^2} \tag{6}$$

where

$$M^{(i)}_{cv} = \langle\psi_v|p_i|\psi_c\rangle. \tag{7}$$

It follows that if $\varepsilon_{out} = \varepsilon_{in}$ (i.e., if $\delta = 1$) the polarization anisotropy in the optical transition is completely determined by the intrinsic anisotropy of the interband dipole matrix elements. If, however, $\delta \neq 1$, there will be a polarization anisotropy component deriving from the discontinuity in the dielectric constant between wire and surrounding material, even in the absence of anisotropy in M_{cv}. This effect vanishes in spherical objects, where the field distribution due to boundary conditions does not depend on the light polarization. A further cause of polarization anisotropy could also arise in case the electric field were inhomogeneously distributed inside the wire[22].

B. Polarization anisotropy due to valence band mixing

1. Band couplings

In bulk zinc-blende semiconductors with point group T_d the valence bands can have three symmetries: Γ_8, Γ_7, and Γ_6. The Γ_{8v} bands are fourfold degenerate at zone center ($k = 0$) and have a total angular momentum $J = 3/2$, with projection along z $J_z = \pm 3/2$ (these

bands are also known as heavy-holes), and $J_z = \pm 1/2$ (these bands are known as light-holes). The Γ_{7v} bands, also called split-off bands, have $J = 1/2$, and $J_z = \pm 1/2$ and are located Δ_{so} below the Γ_{8v} bands at zone center. Group theoretical treatments[16,18,26,28] have long established that the characterization of valence band states as heavy-holes and light-holes is not possible in QWRs, because the irreducible representations for the hole states in these structures (see below) do not transform neither like heavy-hole nor like light-hole, but have a mixed character at all $\mathbf{k}$. One of the main causes of polarization dependence in the optical transitions in QWRs is precisely this mixing of the valence bands. This is in contrast to the case of the quantum well, where the hh and lh states are decoupled at the zone center.

There are two types of possible zone-center coupling between valence bands in a QWR: (i) intra-band coupling between the components (hh, lh) of the bulk Γ_{8v}-derived bands[20]: $\Gamma_{8v}(J_z = 3/2)$–$\Gamma_{8v}(J_z = -1/2)$ and $\Gamma_{8v}(J_z = -3/2)$–$\Gamma_{8v}(J_z = 1/2)$. According to the $\mathbf{k}\cdot\mathbf{p}$ approach[17,19,21], the highest degree of linear polarization produced by this hh-lh coupling for the fundamental $h_1 \rightarrow e_1$ (band gap) transition is 60%, independent of wire diameter and composition[19] or orientation[21]. (ii) Inter-band coupling between the bulk Γ_{8v}-derived lh and the Γ_{7v}-derived split-off bands: $\Gamma_{8v}(J_z = \pm 1/2)$–$\Gamma_{7v}(J_z = \pm 1/2)$. Citrin and Chang showed[28] that, in square cross-section wires, this lh-split-off coupling affects the energy position and dispersion of all subbands at the zone center in QWRs. This is a consequence of the hh-lh coupling (i) in these wires: in quantum wells, where at zone center there is no such hh-lh coupling and the valence subbands can be characterized as pure hh or lh, the heavy-holes do not couple to the split-off bands for $k = 0$[28]; if the hole subbands in a wire had pure hh or lh character, the inclusion of the spin-orbit coupling would influence only lh states, leaving hh states unchanged. As in these wires all energy subbands are affected when spin-orbit is considered, it follows that all states have some lh component, i.e., there is lh-hh coupling. The degree of linear polarization calculated by Citrin and Chang[26] is of the order of 67% in GaAs square cross-section wires. According to Zheng and coworkers[25], the inclusion of the lh-split-off coupling in the $\mathbf{k}\cdot\mathbf{p}$ treatment leads in $In_{0.53}Ga_{0.47}As$ cylindrical wires to a diameter- and temperature-dependent ρ, which ranges from 40% (for a $d = 15$ nm wire at $T = 300$ K) to about 80% (for a $d = 7$ nm wire at the same temperature).

2. *Perceived wire symmetry*

The magnitude of these band couplings and the polarization of the inter-band transitions depend on the symmetry with which the wire is "seen" by a theoretical model. The simplest approach is $\mathbf{k}\cdot\mathbf{p}$, where the wire is assumed to be a *continuous* medium (i.e., with no underlying atomistic structure), modeled as a 2D square well. Within this approach, a circular cross-section wire has therefore an ideally high $C_{\infty v}$ symmetry[19] which is independent of its orientation. However, a real cylindrical wire made of zinc-blende material, due to its underlying atomic structure, has always a lower symmetry than that modeled by the continuum $\mathbf{k}\cdot\mathbf{p}$ approach. Furthermore, this symmetry depends on its crystallographic orientation, or growth direction: if grown along the principal axes [100], [010] or [001] it will have an overall D_{2d} symmetry, otherwise its symmetry will be even lower. A cylindrical wire grown along the (111) direction, for example, has a C_{3v} symmetry. In order to obtain these two symmetries within continuum models, however, one must represent the real circular cross-section wire as having instead square[26,28] (the groups C_{4v} and D_{2d} are isomorphic[33]) and, respectively, triangular[28] cross sections. The problem with the perceived higher symmetry in $\mathbf{k}\cdot\mathbf{p}$ is that the irreducible representations of $C_{\infty v}$ are different from those of the real D_{2d}, C_{3v}, etc. symmetries. This is discussed in the next section.

TABLE I: Summary of the polarizations allowed in $C_{\infty v}$, D_{2d} and C_{4v} symmetry for the different transitions considered. The directions z and x refer to orientations parallel and perpendicular to the wire axis, respectively. The class to which each transition belongs is also indicated: pF and lF stand for parity-Forbidden and l-(angular momentum)-Forbidden; SP and MP stand for Single and Mixed Polarization, respectively.

Irrep.	Transition	Polariz.	Class
$C_{\infty v}$	$C^{(\pm)} \rightarrow E^{(\mp)}$	/	pF
	$C(0) \rightarrow E_{3/2,n}$	x	SP
	$C(0) \rightarrow E_{1/2,n}$	z,x	MP
	$C(1) \rightarrow E_{3/2,n}$	z,x	MP
	$C(1) \rightarrow E_{1/2,n}$	z,x	MP
D_{2d}, C_{4v}	$\Delta l \neq 0$	/	lF
	$\Gamma_6 \rightarrow \Gamma_7$	x	SP
	$\Gamma_7 \rightarrow \Gamma_6$	x	SP
	$\Gamma_6 \rightarrow \Gamma_6$	z,x	MP
	$\Gamma_7 \rightarrow \Gamma_7$	z,x	MP

III. GENERAL PROPERTIES OF WIRES WITH $C_{\infty v}$ AND D_{2d} SYMMETRIES

In a $C_{\infty v}$ wire the irreducible representation of the valence states at Γ are characterized[19] by the value F_z of the z component of their total angular momentum $\mathbf{F} = \mathbf{J} + \mathbf{L}$ (where L is the angular momentum of the envelope part and J the total angular momentum of the Bloch part of the wave function) and by their zone-center parity [even (+), or odd (-)] in the plane perpendicular to the wire, as $E^{(\pm)}_{F_z,n}$, where n refers to the order of the subband for the particular quantum number F_z. The conduction subbands are labeled according to their parity in the plane

perpendicular to the wire (henceforth when referring to "parity" we will always mean parity in the plane perpendicular to the wire), and the value of $|L_z|$, as $C^{(\pm)}(|L_z|)$. In what follows we will consider interband transitions of the form $C^{(\pm)}(|L_z|) \rightarrow E^{(\pm)}_{F_z,n}$ (at zone center, transitions between subbands with different parities, i.e., $C^{(\pm)}(|L_z|) \rightarrow E^{(\mp)}_{F_z,n}$, are forbidden). The allowed transitions can be divided into two general classes, depending on their polarization: (i) mixed polarization (MP) transitions, that have both perpendicular (x) and parallel (z) component (to this class belong $C(0) \rightarrow E_{1/2,n}$, $C(1) \rightarrow E_{1/2,n}$ and $C(1) \rightarrow E_{3/2,n}$[19]); (ii) single polarization (SP) transitions, that are polarized only perpendicular to the wire axis, like $C(0) \rightarrow E_{3/2,n}$[19].

In a C_{4v} square cross-section wire or a D_{2d} cylindrical wire instead, the conduction and valence subbands have Γ_6 and Γ_7 symmetry[28]. In order to determine the allowed and forbidden transitions in D_{2d} wires we can resort to considerations similar to those regarding the conservation of the parity quantum number, just made for $C_{\infty v}$ wires. In this case the angular momentum l of the envelope function needs to be conserved, therefore transitions between subbands with different value of l are *formally* forbidden. This criterion would yield the same forbidden transitions in D_{2d} wires as the parity selection rule yielded in $C_{\infty v}$ wires. However, we find that, due to the strong confinement, the wire subbands do not have pure (s, p, d, etc.) character, but receive contributions from different angular momenta. This leads to a relaxation of the angular momentum conservation rule in D_{2d} cylindrical wires. The interband $\Gamma_i \rightarrow \Gamma_j$ transitions (with $i, j = 6, 7$), can again be grouped into two classes, as before: (i) the mixed polarization transitions include only $\Gamma_i \rightarrow \Gamma_i$ transitions, whereas to (ii) single polarization transitions belong transitions between subbands with different symmetries. The explanation for the inclusion of a particular transition in one of the two classes derives from general group theoretical considerations. In $C_{\infty v}$, C_{4v} and D_{2d} wires, the component of the dipole operator along the z axis transforms as the identity representation[19]. Therefore, in $C_{\infty v}$ wires transitions between conduction subbands with $L_z = 0$ ($C(0)$) and valence subbands with $F_z = 3/2$ cannot occur if the optical wave is polarized along the wire axis z. The same is true for transitions between subbands with different symmetries in C_{4v} and D_{2d} wires. Transitions through optical waves polarized perpendicular to the wire are however allowed. Table I summarizes the allowed polarizations for the different transitions considered and indicates the class to which each transition belongs.

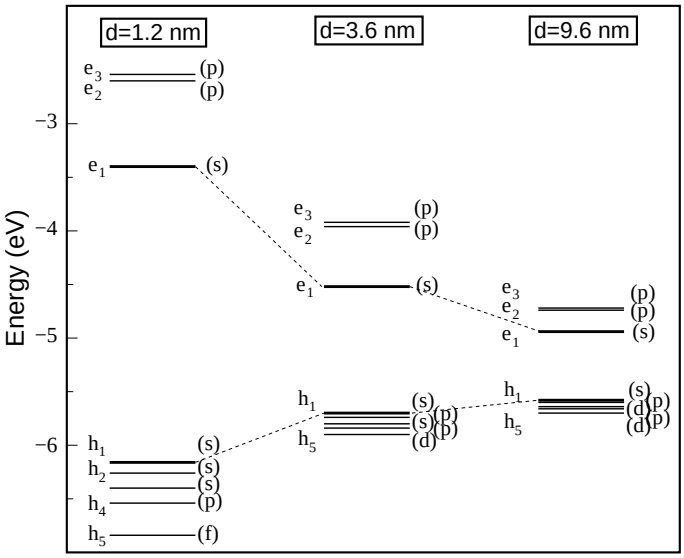

FIG. 1: Schematics of the calculated single-particle energy levels (labeled with their main angular momentum component) for 3 InAs D_{2d} cylindrical wires with sizes $d = 1.2, 3.6, 9.6$ nm respectively. The dashed lines connect respectively CBM and VBM in the different wires. Only a few states are shown that were used in the calculations of the optical properties.

IV. ATOMISTIC DESCRIPTION OF D_{2d} WIRES

The electronic structure of a nanostructure is calculated by solving the single-particle Schrödinger equation:

$$\left[-\frac{\hbar^2}{2m}\nabla^2 + V(\mathbf{r})\right]\psi_i(\mathbf{r}) = \epsilon_i\psi_i(\mathbf{r}), \tag{8}$$

where $V(\mathbf{r})$ is the potential and ϵ_i the energy eigenvalues. In the effective mass approximation, m is taken as the *effective* mass, and $V = V_{ext}(\mathbf{r})$ is an *external* potential defining the geometric confinement of the nanostructure. We use a different approach, where $m = m_0$ is the actual (bare) electron mass and the microscopic pseudopotential of the system $V_{ps}(\mathbf{r})$ is obtained as a superposition of screened atomic potentials,

$$V_{ps}(\mathbf{r}) = \Sigma_{i,\alpha} v_\alpha(\mathbf{r} - \mathbf{R}_{i,\alpha}), \tag{9}$$

where $v_\alpha(\mathbf{r} - \mathbf{R}_{i,\alpha})$ is the atomic potential for an atom of type α located at the position $\mathbf{R}_{i,\alpha}$. The atomic pseudopotentials are derived from the bulk LDA screened pseudopotential and fitted to reproduce the measured InAs bulk transition energies, deformation potentials and effective masses[29]. The total potential is then expressed as

$$V(\mathbf{r}) = V_{ps}(\mathbf{r}) + V_{nl} \tag{10}$$

where V_{nl} accounts for the nonlocal part of the potential and includes the SO coupling. In this atomistic approach Eq. (9) we set up the zinc-blende geometry of

the system (nanostructure plus its surrounding matrix) in a supercell with periodic boundary conditions. The supercell size is chosen so as to minimize any interaction between neighbouring nanostructures This is obtained by increasing the supercell size until the calculated electron ground state energy does not change to within 1 meV (the hole energies converge much faster than the electron energies). We model LCG grown wires as free-standing, unstrained systems. In order to simulate the effect of an oxide coating, that is often present after the wire growth[9], the nanostructures are embedded in a lattice-matched fictitious wide-gap ($\sim$ 5.6 eV) material. This results in large band offsets and the absence of strain between matrix and wire. The atoms occupy therefore the ideal positions of a perfect zinc-blende bulk crystal.

Due to the large number of atoms involved, we solve Eq. (8) by using the *folded spectrum method*[30,31], whereby it is possible to calculate exactly only selected eigenstates of the Schrödinger equation around an arbitrary reference energy $\epsilon_{\rm ref}$. In this approach, Eq. (8) is replaced by:

$$\left[-\frac{\hbar^2}{2m_0}\nabla^2 + V_{ps}(\mathbf{r}) + V_{nl} - \epsilon_{\rm ref}\right]^2 \psi_i(\mathbf{r}) = (\epsilon_i - \epsilon_{\rm ref})^2 \psi_i(\mathbf{r}), \tag{11}$$

which is equivalent to it in the sense that the *ground state* of Eq. (11) coincides with the solution of Eq. (8) with energy closest to $\epsilon_{\rm ref}$. Therefore, with this method the band-edge states can be obtained by choosing the reference energy inside the band gap. The minimization procedure is carried out in a plane-wave basis set using a preconditioned conjugate-gradients algorithm. More details on this procedure can be found in Ref.[31]. With the single-particle energies and wave functions thus obtained, we calculate the inter-band transition energies $E_{cv} = \epsilon_c - \epsilon_v$ and dipole matrix elements:

$$M_{cv}^{(i)} = \langle \psi_v | p_i | \psi_c \rangle \tag{12}$$

where ϵ_v, ψ_v and ϵ_c, ψ_c are valence and conduction band eigenenergies and wave functions, respectively, and $\mathbf{p}$ is the momentum operator with coordinates p_i ($i = x, y, z$). The emission spectrum is then calculated as a function of energy and temperature according to:

$$I_{cv}^{(i)}(E,T) = C \frac{\sum_{c',v'} |M_{c'v'}^{(i)}|^2 \, e^{-\frac{(E-E_{c'v'})^2}{\lambda^2}} e^{-\frac{(E_{c'v'}-E_{cv})}{k_B T}}}{\sum_{c',v'} e^{-\frac{(E_{c'v'}-E_{cv})}{k_B T}}} \tag{13}$$

where C is a constant, λ is the PL broadening, T is the temperature, and we take a Boltzmann average, where the sum over $c'v'$ is over states that satisfy $E_{c'v'} \geq E_{cv}$, to take into account temperature effects.

V. RESULTS

In order to investigate the role of microscopic structure and degree of valence-band coupling in the determination of the wire optical properties, we calculated dipole matrix elements and degree of linear polarization for cylindrical wires with diameters in the range 1–10 nm, both in the finite (W/SO) and in the zero (N/SO) spin-orbit splitting approximation. In this way we were able to vary the mixing between Γ_8-derived and Γ_7-derived bands, which is maximum in the absence of SO interaction.

A. Single-particle energies of cylindrical InAs wires

Figure 1 shows schematically the electron and hole energy levels calculated with our atomistic method, together with their main angular momentum component, relative to 3 InAs wire sizes: the thinnest, $d = 1.2$ nm, the thickest, $d = 9.6$ nm, and an intermediate size, $d = 3.6$ nm. We see that the energy gap and the energy splitting between the subbands decreases with increasing wire diameter, owing to the decreased size confinement effect. As we will see, this feature is one of the causes of the different temperature behaviour of the degree of linear polarization with different wire size.

B. Calculated polarizations and the role of dielectric mismatch

Figures 2 and 3 show the dipole matrix elements squared $|M|^2$ and the relative degree of linear polarization, for the $h_i \rightarrow e_j$ ($i = 1, \ldots, 6$ and $j = 1, 2, 3$) transitions with light polarized along the wire axis (z-polarized) and perpendicular to it (x-polarized). The x- and z-polarized matrix elements relative to the same transition are offset for clarity. The degree of linear polarization shown was calculated from Eq. (6) considering only the anisotropy of the matrix elements but not the dielectric constant discontinuity between wire and surrounding material (i.e., $\delta = 1$). Indeed $\delta \approx 1$ in a wire covered by an oxide, where the two materials have similar dielectric constants. In the case of a free standing wire in vacuum ($\varepsilon_{out} = 1$), because of the small value of δ in Eq. (6), the anisotropy due to the dielectric constant discontinuity dominates over the contribution due to the matrix element anisotropy. Using our calculated matrix elements and the values of $\varepsilon_{in} = 14.6$ for the InAs dielectric constant and $\varepsilon_{out} = 1$, we find that the degree of linear polarization of the fundamental transition $h_1 \rightarrow e_1$ assumes values $> 99\%$ for all wire diameters considered. On the other hand, if we assume isotropic matrix elements ($M^{\perp} = M^{\parallel}$) in Eq. (6), we obtain for the same systems the value of 96.8%. Therefore we find that, for a wire in vacuum, the matrix element anisotropy contributes by less than 3% to the total anisotropy.

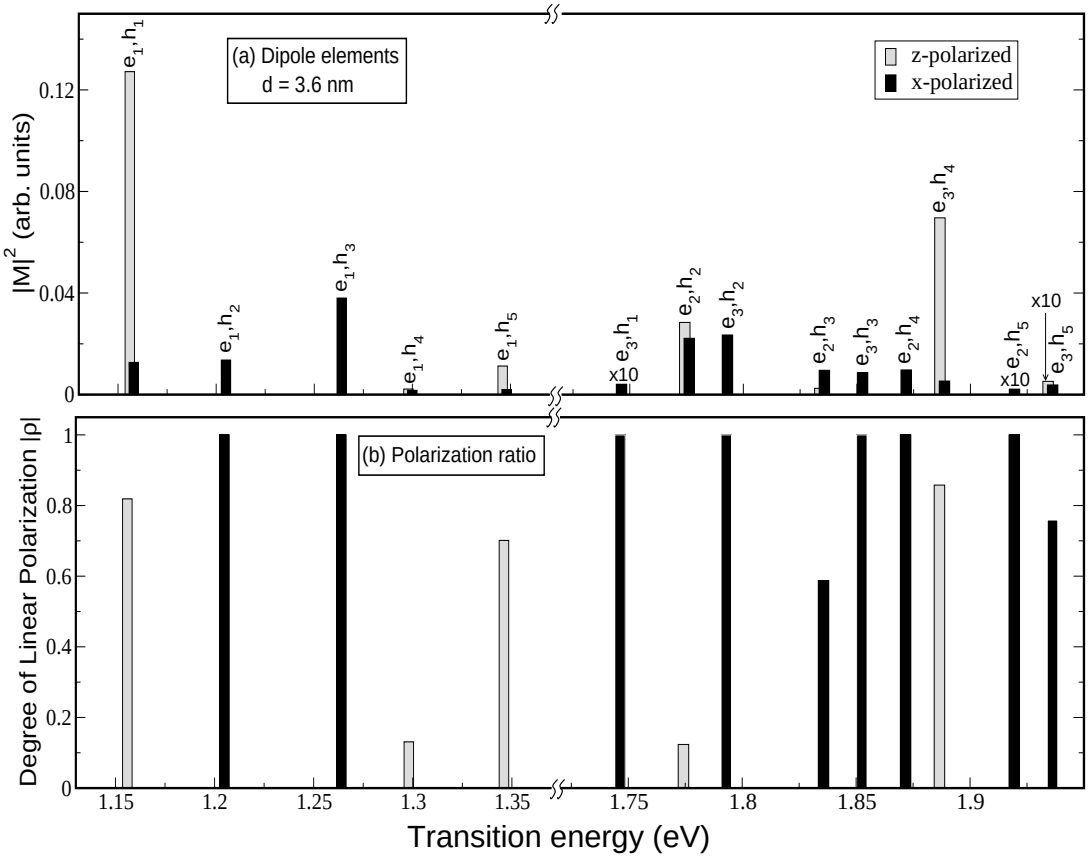

FIG. 2: (a) Matrix elements squared and (b) degree of linear polarization for the interband transitions $h_i \to e_j$ ($i = 1, \ldots, 5$, $j = 1, 2, 3$), as a function of the transition energy for the $d = 3.6$ nm InAs wire.

C. Symmetry considerations

Table II summarizes the irreducible representations of the first 3 conduction and 5 valence subbands in $C_{\infty v}$[19], D_{2d} and C_{4v}[28] wires with similar sizes. In a $C_{\infty v}$ wire the lowest conduction subband $C^{(+)}(0)$ has even parity and is singly degenerate (excluding spin), whereas the next subband $C^{(-)}(1)$ has odd parity and is doubly degenerate (without spin). The uppermost subbands $h_1, \ldots, h_5$ in a $d = 10$ nm wire at zone center are[19]: $E^{(+)}_{1/2,1}$, $E^{(-)}_{1/2,2}$, $E^{(+)}_{3/2,1}$, $E^{(-)}_{3/2,2}$, and $E^{(+)}_{3/2,3}$, respectively. In a $L = 10$ nm C_{4v} square cross-section wire (where L is the square side dimension), instead, the lowest conduction states e_1, e_2 and e_3 have Γ_6[26], Γ_7 and Γ_7 symmetry, respectively. The uppermost valence subbands $h_1, \ldots, h_5$ in this case are[28]: Γ_6, Γ_7, Γ_6, Γ_7, and Γ_7, respectively. In this work we find that, despite the identical labeling between the C_{4v} and D_{2d} representations[33], the ordering of both conduction and valence subbands in a $L = 10$ nm C_{4v} square cross-section and D_{2d} cylindrical wires is different (see Table II). In fact, although the isomorphism between the C_{4v} and D_{2d} groups specifies the possible symmetries of the subbands, it does not pose any constraint on their specific ordering, a feature which depends, among other factors, on the magnitude of the confinement. It is therefore not inconsistent with our group theoretical considerations that the subbands in cylindrical and square cross-section wires have different order. This fact has important consequences on the allowed polarizations in several transitions. From Table II we see that the lowest conduction subband e_1 and the uppermost valence subband h_1 have the same symmetry (and the same main angular momentum component) in C_{4v} and D_{2d} wires. As a consequence, the lowest energy transition has the same polarization (i.e., MP) in both wires. This property can be expected in general from isomorphic groups, and reflects the stability of the band edges with respect to perturbations, such as the change in wire symmetry can be considered to be. Therefore, by considering a continuous wire with the appropriate cross section (i.e. the one that simulates the symmetry resulting from the underlying crystal structure of the real wire, as mentioned in Sec. II B 2), one should always be able to obtain the correct polarization for the ground state transition. As shown in Table II, however, the similarity between two isomorphic groups cannot be exploited further to infer the polarization of higher energy transitions as the ordering of the remaining subbands might be different in the two groups. Given the ordering of the subbands shown in Table II,

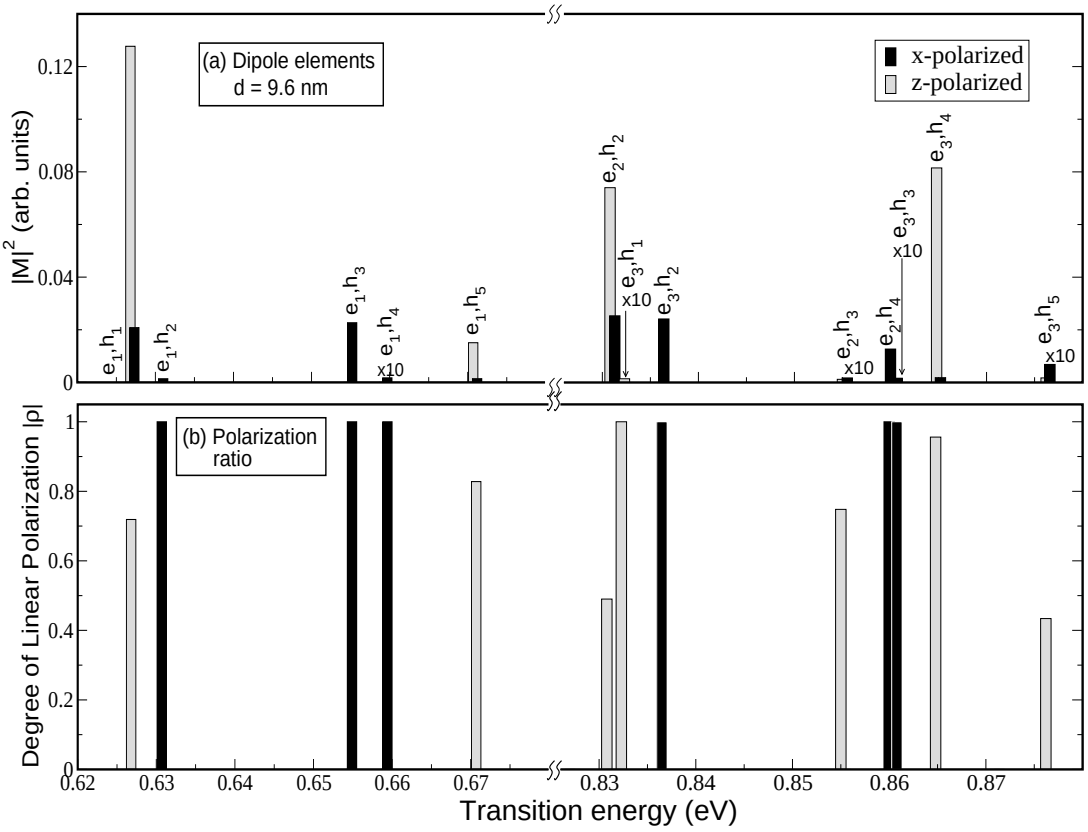

FIG. 3: (a) Matrix elements squared and (b) degree of linear polarization for the interband transitions $h_i \rightarrow e_j$ ($i = 1, \ldots, 5$, $j = 1, 2, 3$), as a function of the transition energy for the $d = 9.6$ nm InAs wire.

TABLE II: Summary of the irreducible representations of the first 5 valence and 3 conduction subbands in wires with $C_{\infty v}$ ($d = 10$ nm), D_{2d} ($d \geq 3.6$ nm) and C_{4v} ($L = 10$ nm) symmetry.

Subband	Representation		
	$C^{(a)}_{\infty v}$	$D^{(b)}_{2d}$	$C^{(c)}_{4v}$
e_1	$C^{(+)}(0)$	Γ_6	Γ_6
e_2	$C^{(-)}(1)$	Γ_7	Γ_7
e_3	$C^{(-)}(1)$	Γ_6	Γ_7
h_1	$E^{(+)}_{1/2,1}$	Γ_6	Γ_6
h_2	$E^{(-)}_{1/2,2}$	Γ_7	Γ_7
h_3	$E^{(+)}_{3/2,1}$	Γ_7	Γ_6
h_4	$E^{(-)}_{3/2,2}$	Γ_6	Γ_7
h_5	$E^{(+)}_{3/2,3}$	Γ_6	Γ_7

[a] Ref.[19]
[b] Present calculation.
[c] Ref.[26,28].

using the general arguments discussed in Section III we can deduce the polarizations allowed in all the transitions involving the first 3 conduction and 5 valence subbands in wires with $C_{\infty v}$, C_{4v} and D_{2d} symmetry. The results are summarized in Table III, which also contains our pseudopotential results. A consequence of the different subband ordering in C_{4v} and D_{2d} symmetry is that transitions with particular polarizations that are forbidden in C_{4v} symmetry are allowed in D_{2d} and vice versa. Furthermore Table III also highlights two other important differences between D_{2d} and C_{4v} wires: (i) the different angular momentum composition of the subbands, which is manifested in different l-forbidden transitions; (ii) the fact that in continuous wires the subbands always have pure l character, as opposed to atomistic wires where, as discussed in Section III, each subband receives contributions from different angular momentum components. The angular momentum selection rule is therefore relaxed in D_{2d} wires and formally forbidden transitions may become weakly allowed. We find that this mixing of l character in the wave functions of D_{2d} wires increases with decreasing wire diameter (i.e., with increasing confinement) and with increasing subband position (i.e., h_5 and e_3 are more mixed than h_1 and e_1). This is reflected in the decrease, with increasing wire diameter, of the magnitude of the optical matrix elements relative to the formally angular-momentum-forbidden transitions (compare Figures 2a and 3a). Furthermore the lower degree of angular momentum component mixing in e_2 compared

to e_3 is shown in the fact that, although both conduction states have main p character (and h_1 main s), the $e_2 \to h_1$ transition is forbidden (see Table III), whereas the $e_3 \to h_1$ transition is very weakly allowed (see Figures 2a and 3a).

TABLE III: Summary of the polarization predicted for the transitions $e_i \to h_j$ ($i = 1, 2, 3$, $h = 1, \ldots, 5$) for wires with (atomistic) D_{2d} ($d1 = 3.6$ nm, $d2 = 9.6$ nm) and (continuum) $C_{\infty v}$ ($d = 10$ nm) and C_{4v} ($L = 10$ nm) symmetry. The main angular momentum components obtained in the present calculation for each subband the are indicated in parenthesis. The directions z and x refer to orientations parallel and perpendicular to the wire axis, respectively. In case of multiple polarizations, the first direction quoted is the one with the largest matrix element. We indicate in boldface the polarizations that are found different between $d1$ and $d2$ for the same transition. Each transition is also labeled by the class to which it belongs, according to Table I.

Transition	Polarization			
	EPM		**k·p**	
	D_{2d}(d1)	D_{2d}(d2)	$C^{(a)}_{\infty v}$	$C^{(b)}_{4v}$
e_1(s)→ h_1(s)	z,x(MP)	z,x(MP)	z,x(MP)	z,x(MP)
e_1(s)→ h_2(p)	x(SP)	x(SP)	pF	x(SP)
e_1(s)→ h_3(s,d)*	x(SP)	x(SP)	x(SP)	lF
e_1(s)→ h_4(p)	**z,x**(MP)	**x**(MP)	pF	lF
e_1(s)→ h_5(d,s)*	z,x(MP)	z,x(MP)	x(SP)	x(SP)
e_2(p)→ h_1(s)	lF	lF	pF	lF
e_2(p)→ h_2(p)	z,x(MP)	z,x(MP)	z,x(MP)	lF
e_2(p)→ h_3(s,d)*	**x,z**(MP)	**z,x**(MP)	pF	x(SP)
e_2(p)→ h_4(p)	x(SP)	x(SP)	z,x(MP)	z,x(MP)
e_2(p)→ h_5(d,s)*	**x**(SP)	**lF**	pF	lF
e_3(p)→ h_1(s)	**x**(MP)	**z**(MP)	pF	lF
e_3(p)→ h_2(p)	x(SP)	x(SP)	z,x(MP)	lF
e_3(p)→ h_3(s,d)*	x(SP)	x(SP)	pF	x(SP)
e_3(p)→ h_4(p)	z,x(MP)	z,x(MP)	z,x(MP)	z,x(MP)
e_3(p)→ h_5(d,s)*	**x,z**(MP)	**z,x**(MP)	pF	lF

* The angular momentum components s and d have similar magnitudes.

[a] Ref.[19]

[b] The polarization of $e_1 \to h_j$ transitions is from Ref.[26], that of transitions involving e_2 and e_3 has been deduced from group theory arguments.

D. Near band-gap transitions $h_i \to e_1$

The fundamental band-gap $h_1 \to e_1$ transition has both z and x polarizations, but is mainly polarized along the wire axis in all wire symmetries considered in Table III. We find that, in the absence of SO interaction ($\Delta_{so} = 0$ eV), in a circular cross-section wire with atomistic D_{2d} symmetry it is 100% z-polarized (i.e., the h_1 state does not interact at all with optical waves polarized normal to the wire axis). When the coupling between bulk Γ_{8v}- and Γ_{7v}-derived valence bands is restored

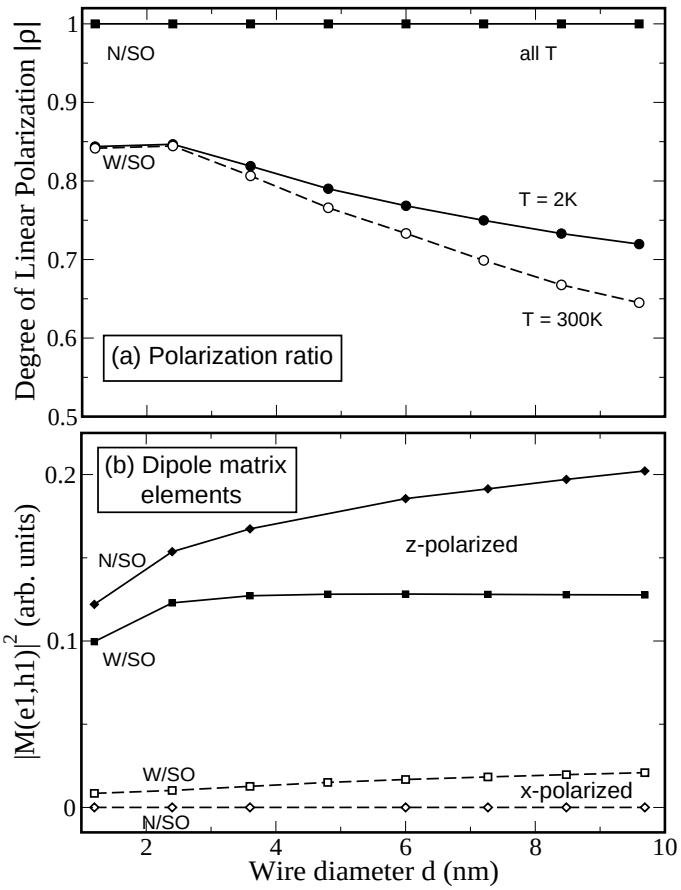

FIG. 4: (a) Degree of linear polarization of the fundamental transition $h_1 \to e_1$ as a function of wire diameter, calculated at $T = 2$ K and $T = 300$ K both considering (W/SO) and not considering (N/SO) SO splitting. (b) Dipole matrix elements, for the same transition, polarized parallel (z) and perpendicular (x) to the wire axis, in the finite and zero SO splitting approximations.

to its actual value (with $\Delta_{so} = 0.4$ eV in bulk InAs) the degree of linear polarization decreases by about 20% and becomes size and temperature dependent. Figures 4 and 5 show the temperature dependence of our calculated dipole matrix elements and degree of linear polarization in the finite and zero SO approximations. This decrease of ρ from 100% to about 80% with increasing SO splitting, together with the value of 60% obtained for ρ in the infinite spin-orbit approximation[17,19,21], show that linear polarization effects in actual 1D systems are due to substantial mixing between the four bulk Γ_{8v}- *and* the two Γ_{7v}-derived valence bands.

The next transition ($h_2 \to e_1$), is a $\Gamma_7 \to \Gamma_6$ transitions in both D_{2d} and C_{4v} wires and is therefore allowed to be polarized only perpendicular to the wire axis. The $h_2 \to e_1$ and the $h_4 \to e_1$ transitions are forbidden in $C_{\infty v}$[19] QWRs, due to the different parity of the electron and hole wave functions. As discussed above, these transitions would be formally (angular-momentum) forbidden in our D_{2d} wires as well. However, due to the non

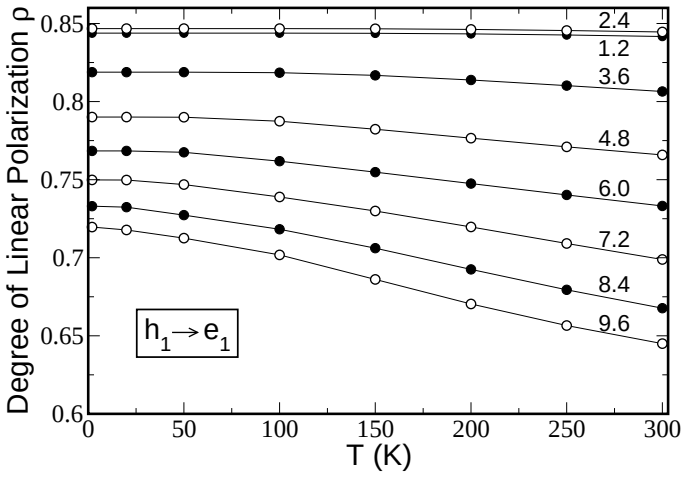

FIG. 5: Degree of linear polarization of the fundamental transition $h_1 \rightarrow e_1$ as a function of temperature T for the different wire diameters considered.

zero $l = 1$ component of e_1 we find that they are weakly allowed: the dipole matrix elements for these transitions decrease by over one order of magnitude with increasing wire diameter (i.e., with decreasing l mixing in e_1), from 2.4 nm to 9.6 nm (both becoming less than 1% of the value of the matrix element relative to the band gap transition in the $d = 9.6$ nm wire). As the $h_3 \rightarrow e_1$ transition is only x-polarized in $C_{\infty v}$ wires, the two lowest energy transitions have opposite polarizations in D_{2d}, C_{4v}, and $C_{\infty v}$ wires. The fundamental transition is in fact polarized mainly along the wire axis while the next allowed transition has only x polarization in all symmetries. The $h_4 \rightarrow e_1$ transition, instead, being a transition between two Γ_6 subbands, can have both polarizations: however, in $d > 4.8$ nm D_{2d} structures, it is only polarized perpendicular to the wire. The polarization component parallel to the wire axis increases from zero[34] to a value which is larger than that of the perpendicular component, when the wire diameter decreases from 9.6 nm to 3.6 nm.

1. *Temperature dependence*

We find (Fig. 4 and Fig. 5) a stronger temperature dependence for $\rho(h_1 \rightarrow e_1)$ in thick wires: in a $d = 9.6$ nm wire ρ decreases by 10% with a 300 K temperature increase, compared to a 0.25% decrease in a $d = 1.2$ nm wire, for the same temperature variation. This size dependence of the polarization can be understood in terms of lateral confinement effects. Due to the quantum size effect, thin wires experience a stronger confinement than thicker wires, which means that they have a higher kinetic energy introduced by the confinement. As this kinetic energy is responsible for the mixing[20] of the valence bands at zone center, thin wires have also a stronger mixing and therefore a higher degree of linear polarization. Furthermore, due to the larger confinement, the hole energy levels are farther apart in thin wires than they are in thicker wires (see Fig. 1), and their density of states is lower close to the band edge. Therefore in thin wires at low temperature the $h_1 \rightarrow e_1$ transition is the most probable and the degree of polarization is high (see Fig. 6). In the case of thick wires the probability for $h_{2,3} \rightarrow e_1$ transitions, which as we mentioned before, unlike the $h_1 \rightarrow e_1$ transition are polarized only perpendicular to the wire, increases with T. This reduces the degree of linear polarization with increasing temperature in thick wires. This is clearly seen in Fig. 6, where we show the PL polarization spectra (with 50 meV broadening) around the energy of the fundamental $h_1 \rightarrow e_1$ transition, calculated at $T = 2$ K and $T = 300$ K for a $d = 1.2$ nm and a $d = 9.6$ nm wire. The different density of states also explains the larger blue shift (7 meV) of the x-polarized PL that takes place in thick wires with a temperature increase of 300 K, compared to that (2 meV) occurring in thin wires (Figure 6). The detectability of PL polarization peaks in these wires is, however, closely related to the experimental line broadening. As shown in Fig. 7, if the broadening is larger than 20 meV at room temperature (in typical experimental conditions it is > 50 meV[1]), the peak in the x-polarized emission corresponding to the $h_3 \rightarrow e_1$ transition, found in Fig. 3, is masked by the broadening of the fundamental transition in a $d = 9.6$ nm wire. In a $d = 1.2$ nm wire (Fig. 7), even if the broadening is of the order of 40 meV, the second peak in the x-polarized emission can still be seen as a shoulder on the high energy side of the main peak, but is almost completely lost in it for broadenings ≥ 50 meV. Therefore this peak has not been seen in cylindrical LCG wires of any size, due to the present experimental accuracy.

E. Higher energy transitions $h_i \rightarrow e_{2,3}$

The $h_1 \rightarrow e_2$ transition is found to be forbidden in all wires considered in Table III. The $h_2 \rightarrow e_2$ and $h_3 \rightarrow e_2$ transitions in Fig. 2 ($\Gamma_7 \rightarrow \Gamma_7$ transitions in D_{2d} wires) are both x- and z-polarized. The former transition has a stronger parallel component that increases with wire diameter, while the perpendicular component stays almost constant. In the $h_3 \rightarrow e_2$ transition (weakly allowed only because of the non zero $l = 2$ component of the e_2 subband in D_{2d} wires, and parity-forbidden in $C_{\infty v}$[19] wires), instead, the perpendicular component decreases by more than one order of magnitude with increasing d, becoming smaller than the parallel component for $d > 3.6$ nm (see Table III). The $h_4 \rightarrow e_2$ and $h_5 \rightarrow e_2$ transitions are $\Gamma_6 \rightarrow \Gamma_7$ transitions in D_{2d} QWRs and can, therefore, only be x-polarized. The former, however, is predicted to have both polarizations in $C_{\infty v}$[19] QWRs, where the $\parallel$ component is the strongest. The $h_5 \rightarrow e_2$ transition that we only find very weakly allowed in small ($d \leq 6$ nm) D_{2d} wires, due to the higher l mixing in these structures, is also formally parity-forbidden in the lower symmetry wires. Interestingly, the (very weakly allowed in

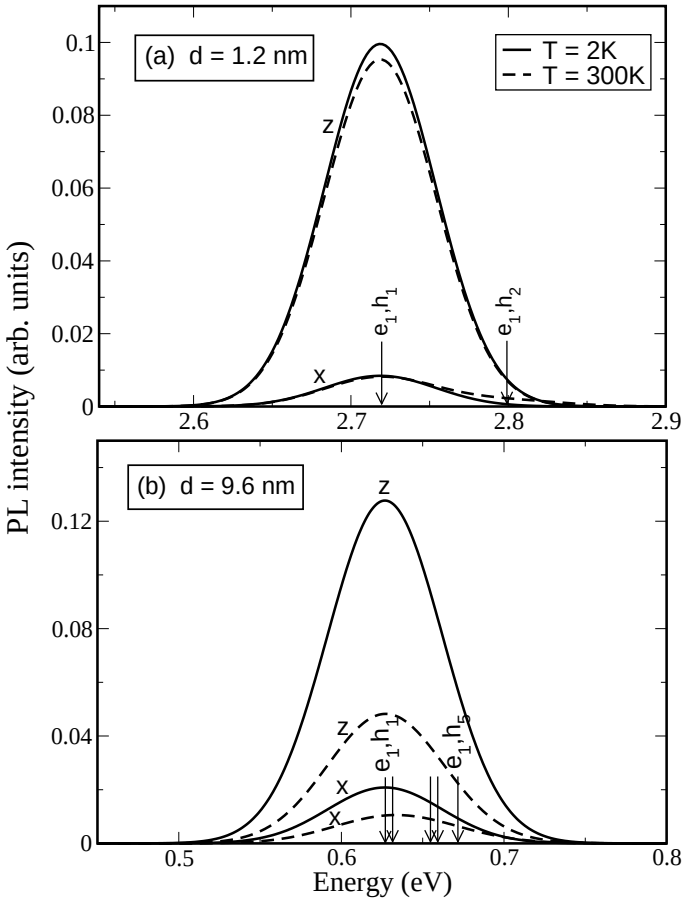

FIG. 6: PL polarization spectra around the energy of the fundamental $h_1 \rightarrow e_1$ transition, calculated at $T = 2$ K and $T = 300$ K for a (a) $d = 1.2$ nm and a (b) $d = 9.6$ nm wire (with 50 meV broadening). The arrows mark the position in energy of the transitions $h_i \rightarrow e_1$, with $i = 1, \ldots, 5$.

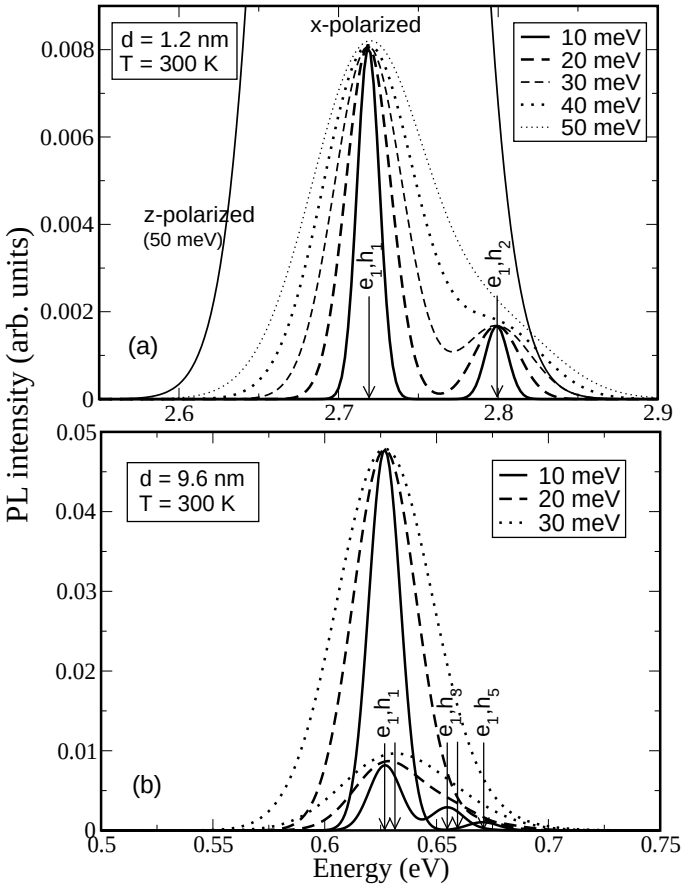

FIG. 7: PL polarization spectra at $T = 300$ K calculated for a $d = 1.2$ nm (a), and a $d = 9.6$ nm (b) wire for different values of the line broadening.

D_{2d} wires) $h_1 \rightarrow e_3$ and $h_5 \rightarrow e_3$ transitions, forbidden in low symmetry wires[19] have opposite polarizations in the two wires of Fig. 2: $h_1 \rightarrow e_3$ is z-polarized in $d > 6$ nm wires and x-polarized in $d \leq 6$ nm wires; in $h_5 \rightarrow e_3$ both polarizations are present, but the $\perp$ component decreases with increasing d, becoming smaller than the $\parallel$ component for $d > 6$ nm.

As a rule we find that whenever a transition is formally angular-momentum-forbidden in D_{2d} QWRs (and parity-forbidden in lower symmetry wires), the $\perp$ component decreases (very often by more than one order of magnitude) with increasing d in D_{2d} QWRs, resulting either very weak or non existent altogether in thick wires.

F. In-plane optical anisotropies

In an attempt to include microscopic features in the **k·p** treatment in the infinite spin-orbit splitting approximation, Yamaguchi and Usui[21] derived a crystallographic-orientation-dependent expression for the dipole matrix element, which led to an in-plane anisotropy. In the spherical approximation for the valence bands (in which the Luttinger parameter $\gamma_2 = \gamma_3$) there is no polarization anisotropy in the plane normal to the wire axis in a $C_{\infty v}$ wire[21]. By including the effect of valence-band anisotropy, Yamaguchi and Usui[21] predicted a weak dependence on the wire orientation for the polarization along z, and a strong dependence for the polarization along two perpendicular directions x and y (both in-plane) for the fundamental transition in wires oriented in directions different than [001] and [111]. Furthermore, only for [001]- and [111]-oriented wires they found no in-plane anisotropy, i.e., $|M^x| = |M^y|$. For all other orientations the calculated dipole matrix elements along x and y were different.

Similarly, we find no in-plane anisotropy in the fundamental transition in D_{2d} wires. However, higher energy transitions show polarization anisotropy in the plane perpendicular to the wire axis. Figures 8 and 9 show the xy-plane ($\perp$ to the wire axis) anisotropy we find in the $h_4 \rightarrow e_1$ and $h_5 \rightarrow e_1$ transitions in D_{2d} QWRs, grown along the [001] direction, with $d \geq 6$ nm, where the matrix element along the [110] direction is different

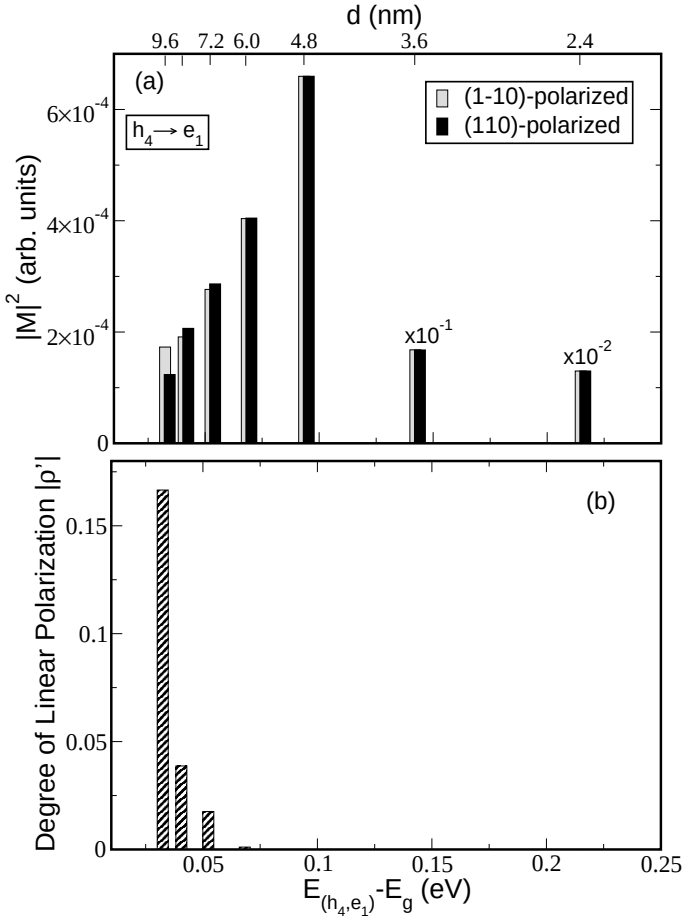

FIG. 8: (a) In-plane matrix elements squared and (b) degree of linear polarization for the interband transitions $h_4 \rightarrow e_1$, as a function of the transition energy measured from the band gap (lower x axis) and wire diameter (upper x axis), in D_{2d} InAs wires.

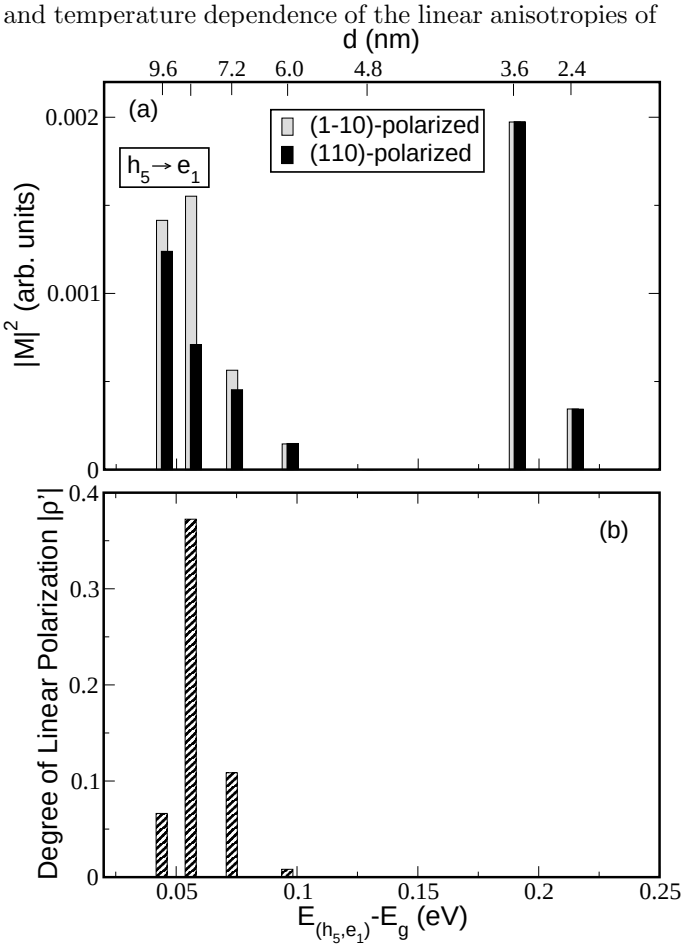

FIG. 9: (a) In-plane matrix elements squared and (b) degree of linear polarization for the interband transitions $h_5 \rightarrow e_1$, as a function of the transition energy measured from the band gap (lower x axis) and wire diameter (upper x axis), in D_{2d} InAs wires.

from that along the $[1\bar{1}0]$ direction. We see that the $h_4 \rightarrow e_1$ transition is prevalently [110]-polarized with only the $d = 9.6$ nm wire polarized along $[1\bar{1}0]$. The opposite is true for the $h_5 \rightarrow e_1$ transition, where the only size for which the transition is prevalently polarized along [110] is $d = 6$ nm. However the $d = 9.6$ nm wire is found mainly polarized along $[1\bar{1}0]$ and the $d = 6$ nm wire mainly along [110], in both transitions. In all other transitions considered we found no anisotropy in the xy plane.

VI. SUMMARY

In summary we applied an atomistic, empirical pseudopotential method to calculate optical transitions in free-standing, unstrained [001]-oriented cylindrical InAs quantum wires with diameters in the experimentally accessible range 10-100 Å. We found evidence of strong coupling of bulk Γ_{8v}- and bulk Γ_{7v}-derived bands in the size and temperature dependence of the linear anisotropies of optical transitions in QWRs. We show that simple approaches, that model the wire as a continuum with no underlying crystal structure, miss some optical transitions, due to their strict application of conservation rules that we found to be relaxed in strongly confined atomistic nanostructures.

VII. ACKNOWLEDGMENTS

The authors thank G. Bester for many valuable comments and suggestions and for his accurate reading of the manuscript.

This work was supported by the U.S. DOE-SC-BES, Division of Materials Science, under the Nanoscience Initiative DOE LAB 03-17.

[1] J. Wang, M. S. Gudiksen, X. Duan, Yi Cui, C. M. Lieber, Science 293, 1455 (2001).

[2] Yu Huang, X. Duan, Q. Wei, C. M. Lieber, Science 291, 630 (2001).

[3] M. S. Gudiksen, J. Wang, and C. M. Lieber, J. Phys. Chem. **105**, 4062 (2001).

[4] Y. Wu and P. Yang, J. Am. Chem. Soc. **123**, 3165 (2001).

[5] Yi Cui, L. J. Lauhon, M. S. Gudiksen, J. Wang and C. M. Lieber, Appl. Phys. Lett. **78**, 2214 (2001); X. Duan, J. Wang, and C. M. Lieber, Appl. Phys. Lett. **76**, 1116 (2000).

[6] X. Duan and C. M. Lieber, J. Am. Chem. Soc. 122, 188 (2000); M. S. Gudiksen and C. M. Lieber, J. Am. Chem. Soc. **122**, 8801 (2000).

[7] X. Duan and C. M. Lieber, Adv. Mater. **12**, 298 (2000).

[8] J. Hu, T. W. Odom, and C. M. Lieber, Acc. Chem. Res. **32**, 435 (1999).

[9] A. M. Morales and C. M . Lieber, Science **279**, 208 (1998).

[10] E. Kapon, D. M. Hwang, R. Bhat, Phys. Rev. Lett. **63**, 430 (1989).

[11] M. Tsuchiya, J. M. Gaines, R. H. Yan, R. J. Simes, P. O. Holtz, L. A. Coldren, P. M. Petroff, Phys. Rev. Lett. **62**, 466 (1989).

[12] M. Kohl, D. Heitmann, P. Grambow, K. Ploog, Phys. Rev. Lett. **63**, 2124 (1989).

[13] H. Akiyama, T. Someya, H. Sakaki, Phys. Rev. B **53**, R4229 (1996).

[14] T. Sogawa, H. Ando, S. Ando, H. Kanbe, Phys. Rev. B **56**, 1958 (1997).

[15] F. Vouilloz, D. Y. Oberli, M.-A. Dupertuis, A. Gustafsson, F. Reinhardt, E. Kapon, Phys. Rev. Lett. **78**, 1580 (1997).

[16] J. A. Brum and G. Bastard, Superlatt. Microstruct. **4**, 443 (1988).

[17] P. C. Sercel and K. J. Vahala, Appl. Phys. Lett. **57**, 545 (1990).

[18] P. C. Sercel and K. J. Vahala, Phys. Rev. B **42**, 3690 (1990).

[19] P. C. Sercel and K. J. Vahala, Phys. Rev. B **44**, 5681 (1991).

[20] U. Bockelmann and G. Bastard, Phys. Rev. B **45**, 1688 (1992).

[21] A. A. Yamaguchi and A. Usui, J. Appl. Phys. **78**, 1361 (1995).

[22] P. Ils, Ch. Greus, A. Forchel, V. D. Kulakovskii, N. A. Gippius, S. G. Tikhodeev, Phys. Rev. B **51**, 4272 (1995).

[23] E. A. Muljarov, E. A. Zhukov, V. S. Dneprovskii, Y. Masumoto, Phys. Rev. B **62**, 7420 (2000).

[24] M. A. Dupertuis, E. Martinet, D. Y. Oberli, E. Kapon, Europhys. Lett. **52**, 420 (2000).

[25] W. H. Zheng, J.-B. Xia, K. W. Cheah, J. Phys. Condens. Matter **9**, 5105 (1997).

[26] D. S. Citrin, Y.-C. Chang, J. Appl. Phys. **70**, 867 (1991).

[27] G. Bester, S. Nair. A. Zunger, Phys. Rev. B *67*, 161306 (2003).

[28] D. S. Citrin and Y.-C. Chang, Phys. Rev. B **40**, 5507 (1989).

[29] L. W. Wang and A. Zunger, Phys. Rev. B **51**, 17 398 (1995); H. Fu and A. Zunger, Phys. Rev. B **56**, 1496 (1997).

[30] L. W. Wang and A. Zunger, J. Chem. Phys. **100**, 2394 (1994); J. Phys. Chem. **98**, 2158 (1994).

[31] L. W. Wang and A. Zunger, in *Semiconductor Nanoclusters*, edited by P. V. Kamat and D. Meisel (Elsevier, New York, 1996).

[32] L. D. Landau and E. M. Lifshitz, *Electrodynamics of continuous media*, (Moscow, Nauka 1992).

[33] G. F. Koster, J. O. Dimmock, R. G. Wheeler, H. Slatz, *Properties of the Thirty-Two Point Groups* (MIT Press, Cambridge, Mass., 1966).

[34] We assume a matrix element $|M^{(i)}|^2$ $(i = \|, \perp)$ to be zero when its value is $\lesssim 10^{-4}|M^{\|}_{e1,h1}|^2$.

[35] W. T. Masselink, Y.-C. Chang, H. Morkoc, Phys. Rev. B **32**, 5190 (1985).